



HAL
open science

Constraints on Planetesimal Accretion Inferred from Particle-size Distribution in CO Chondrites

Gabriel A Pinto, Yves Marrocchi, Alessandro Morbidelli, Sébastien Charnoz, Maria Eugenia Varela, Kevin Soto, Rodrigo Martínez, Felipe Olivares

► **To cite this version:**

Gabriel A Pinto, Yves Marrocchi, Alessandro Morbidelli, Sébastien Charnoz, Maria Eugenia Varela, et al.. Constraints on Planetesimal Accretion Inferred from Particle-size Distribution in CO Chondrites. The Astrophysical journal letters, 2021, 917 (2), pp.L25. 10.3847/2041-8213/ac17f2 . hal-03368922

HAL Id: hal-03368922

<https://hal.science/hal-03368922>

Submitted on 7 Oct 2021

HAL is a multi-disciplinary open access archive for the deposit and dissemination of scientific research documents, whether they are published or not. The documents may come from teaching and research institutions in France or abroad, or from public or private research centers.

L'archive ouverte pluridisciplinaire **HAL**, est destinée au dépôt et à la diffusion de documents scientifiques de niveau recherche, publiés ou non, émanant des établissements d'enseignement et de recherche français ou étrangers, des laboratoires publics ou privés.

Constraints on planetesimal accretion inferred from particle-size distribution in CO chondrites

Gabriel A. Pinto^{1,2,*}, Yves Marrocchi¹, Alessandro Morbidelli³, Sébastien Charnoz⁴, Maria Eugenia Varela⁵, Kevin Soto⁶, Rodrigo Martínez⁷ & Felipe Olivares²

¹Université de Lorraine, CNRS, CRPG, UMR 7358, Vandœuvre-lès-Nancy, 54501, France

²Instituto de Astronomía y Ciencias Planetarias, Universidad de Atacama, Copayapu 485, Copiapó, Chile

³Laboratoire Lagrange, UMR7293, Université de Nice Sophia-Antipolis, CNRS, Observatoire de la Côte d'Azur, Boulevard de l'Observatoire, F-06304 Nice Cedex4, France

⁴Université de Paris, Institut de physique du globe de Paris, CNRS, F-75005 Paris, France

⁵Instituto de Ciencias Astronómicas, de la Tierra y el Espacio, ICATE-CONICET, San Juan, Argentina

⁶Facultad de Ciencias, Instituto de Ciencias de la Tierra, Universidad Austral de Chile, Valdivia, Chile

⁷Museo del Meteorito, San Pedro de Atacama, Chile

*Corresponding author: gabriel.pinto@univ-lorraine.fr

Abstract

The formation of planetesimals was a key step in the assemblage of planetary bodies, yet many aspects of their formation remain poorly constrained. Notably, the mechanism by which chondrules—sub-millimetric spheroids that dominate primitive meteorites—were incorporated into planetesimals remains poorly understood. Here we classify and analyze particle-size distributions in various CO carbonaceous chondrites found in the Atacama Desert. Our results show that the average circle-equivalent diameters of chondrules define a positive trend with the petrographic grade, which reflects the progressive role of thermal metamorphism within the CO parent body. We show that this relationship could not have been established by thermal metamorphism alone but rather by aerodynamic sorting during accretion. By modeling the self-gravitational contraction of clumps of chondrules, we show that (i) the accretion of the CO parent body(ies) would have generated a gradual change of chondrule size with depth in the parent body, with larger chondrules being more centrally concentrated than smaller ones, and (ii) any subsequent growth by pebble accretion would

34 have been insignificant. These findings give substantial support to the view that planetesimals
35 formed via gravitational collapse.

36

37 **Keywords:** Accretion, Asteroids, Carbonaceous chondrites, Protoplanetary disk,
38 Planetesimals

39

40

41

42

43

44

45

46

47

48

49

50

51

52

53

54

55

56

57

58

59

60 **1. Introduction**

61 Planetesimals are solid objects larger than 1 km in diameter that formed by the
62 accumulation of orbiting bodies in the protoplanetary disk and whose internal strengths are
63 dominated by self-gravity; they represent the main building blocks of the planets orbiting the
64 Sun today. Chondrites are fragments of asteroids that were never sufficiently heated to melt
65 their constituent silicates and thus preserve primitive grains of the materials from which they
66 agglomerated, including refractory inclusions and chondrules, cemented together by a
67 complex fine-grained matrix. Refractory inclusions are millimeter- to centimeter-sized
68 particles that represent the oldest dated objects in the solar system (Connelly et al. 2016).
69 Chondrules are (sub-)millimeter-sized igneous spherules that formed by a still elusive high-
70 temperature mechanism linked to either nebular or planetary processes (e.g., Johnson et al.
71 2015; Marrocchi et al. 2018, 2019). Although chondrules are the main constituents of
72 chondrites and their accretion thus represents a key step in the formation of planetesimals, the
73 mechanism by which they assembled into planetesimals remains poorly constrained.

74 Recent theoretical advances suggest that planetesimals formed from clumps of small
75 particles (mostly chondrules in the case of chondrites) whose common gravitational attraction
76 outweighed the dispersive action of turbulent diffusion (Klahr & Schreiber 2020, 2021). This
77 process requires that clumps of particles be sufficiently dense and massive and would
78 produce planetesimals of typically ~10 - 100 km in diameter depending on the remaining gas
79 mass in the solar nebula at the time of planetesimal formation. However, the formation of
80 such particle clumps remains debated.

81 For instance, it was proposed that particles were concentrated into large vortices
82 (Barge & Sommeria 1995) or in regions between small vortices that developed in the disk at
83 the dissipation scale (Cuzzi et al. 2001, 2008). More recently, it was proposed that particle

84 clumps formed due to *streaming instabilities*, hydrodynamic instabilities due to the
85 differential velocities of particles relative to the surrounding gas (Youdin & Goodman 2005;
86 Johansen et al. 2009; Simon & Armitage 2014; Wahlberg Jansson & Johansen 2014, 2017;
87 Johansen et al. 2015; Li et al. 2018, 2019).

88 For all these scenarios, the effectiveness of streaming instabilities in promoting clump
89 formation depends on particle size, or rather the Stokes number, which here is the ratio
90 between a particle's stopping time due to friction with the gas and the orbital period. For
91 chondrule-sized particles, triggering the gravitational collapse of a pebble cloud in streaming
92 instability (Gerbig et al., 2020) requires particles to be radially concentrated in an annulus
93 (Drażkowska et al. 2016) to achieve a sufficiently large solid/gas ratio (Carrera et al. 2015;
94 Yang et al. 2017). One of the strengths of the gravitational collapse scenarios is that it
95 predicts the formation of binary planetesimals, which are observed in large numbers in the
96 relatively pristine trans-Neptunian belt, and reproduces the observed statistics of their orbital
97 orientations (Nesvorný et al. 2019).

98 Once planetesimals have formed, they can continue growing by accreting individual
99 particles (if they exceed a critical size of about 1000 km diameter, Ormel & Klahr 2010) as
100 they drift through the disk. This process is known as pebble accretion (Lambrechts &
101 Johansen 2012; Johansen et al. 2015). The initial gravitational contraction of a clump of
102 particles and later pebble accretion should produce characteristic variations of particle size
103 with depth inside the resulting planetesimal. Here we report estimated particle-size
104 distributions within different CO carbonaceous chondrites, chosen because they experienced
105 limited alteration processes after their agglomeration, which could have affected the sizes of
106 their constituent particles. We use our data to model the conditions of planetesimal accretion
107 within the protoplanetary disk and the possible layered structure of the CO parent body(ies).

108

109 **2- Material and method**

110 We surveyed all particles in sections of three CO3 carbonaceous chondrites recovered
111 in the Atacama Desert and provided by the Museo del Meteorito (San Pedro de Atacama,
112 Chile): El Médano 216 (EM 216), El Médano 463 (EM 463) and Los Vientos 123 (LoV 123).
113 We also determined the particle-size distribution in Isna (thick section 3239 from the
114 Muséum national d'Histoire naturelle, Paris, France). Backscattered electron (BSE) mosaics
115 and X-ray compositional maps (Fe, Ni, Al, Mg, Ca, Si, S, Cr) were acquired using (i) a JEOL
116 JSM-6510 scanning electron microscope (SEM) equipped with a Genesis EDX detector and
117 operating with a 3 nA electron beam accelerated at 20 kV (CRPG, Nancy, France) and (ii) a
118 JEOL 6400 SEM operating with a 1 nA electron beam accelerated at 15 kV
119 (Naturhistorisches Museum, Vienna, Austria). The chemical compositions of ferroan olivine
120 grains in FeO-rich chondrules of EM 216 and EM 463 were quantified using a Cameca
121 SX100 electron microprobe at the Service Commun de Microscopies Electroniques et de
122 Microanalyses X (SCMEM, Université de Lorraine, Nancy, France) using a 12 nA focused
123 beam accelerated at 15 kV. LoV 123 was analyzed by wavelength dispersive spectroscopy
124 with an ARL-SEMQ electron microprobe at ICATE (San Juan, Argentina) operating with a
125 15 nA electron beam accelerated at 15 kV. Natural and synthetic standards were used for both
126 instrument calibrations.

127 Mosaics of all samples were prepared using the GNU image manipulation program.
128 Particle-size measurements were performed using the Fiji distribution of the ImageJ open-
129 source image processing software (Schindelin et al. 2012). We analyzed all nebular
130 components, including chondrules (types I and II being FeO-poor and -rich, respectively),
131 calcium aluminum-rich inclusions (CAIs, types A and B), amoeboid olivine aggregates
132 (AOAs), and isolated olivine grains (IOGs) over total surface areas of 96 mm², 27 mm², 32.4
133 mm², and 30.6 mm² for EM 463, EM 216, LoV 123, and Isna, respectively. The sharpness

134 and continuity of the borders in the X-ray compositional maps was improved in Fiji by first
135 applying mean filter at 1 pixel and then enhancing the image contrast at 0.5%. Each particle
136 was recorded in a mask layer by free-hand tracing (Fig. 1). We did not distinguish between
137 AOAs or type-A or -B CAIs for refractory components in EM 216 and LoV 123. Each
138 particle's diameter (d) was calculated assuming that its total area was circular in cross section
139 (i.e., as $d = \sqrt{\text{pixel area}/\pi \times 2}$).

141 **3-Results**

142 The Cr₂O₃ contents of subhedral FeO-rich olivine crystals were determined for 43, 49,
143 and 62 type-II porphyritic chondrules in EM 216, EM 463, and LoV 123, respectively.
144 Chondrule olivine grains appear heterogeneous in both texture (Fig. 1) and composition
145 (Fa_{21.3–88.2}, mean Fa_{50.2 ± 10.7}; Table S1). Ferroan olivines in type-II chondrules of EM 463
146 contain 0.04–0.57 wt.% Cr₂O₃ (average 0.09 ± 0.10 wt.%, 1σ, Table S1); those of EM 216
147 and LoV 123 contain 0.09 ± 0.10 and 0.30 ± 0.13 wt.% Cr₂O₃, respectively (Table S1).

148 EM 216, EM 463, and LoV 123 show high modal abundances of FeO-poor type-I
149 chondrules (41.59, 33.15, and 46.74%, respectively, Table 1) surrounded by fine-grained Fe-
150 rich matrix (Fig. 1). Isna is dominated by type-II chondrules (33.26%) with occasional type-I
151 chondrules (1.85%, Table 1). The modal abundances of refractory inclusion (CAIs + AOAs)
152 range from 1.59% in Isna to 8.60% in LoV 123 (Table 1). We also observe a large variation
153 in the modal abundances of type-II chondrules, from 5.22% in EM 216 to 33.26% in Isna
154 (Table 1).

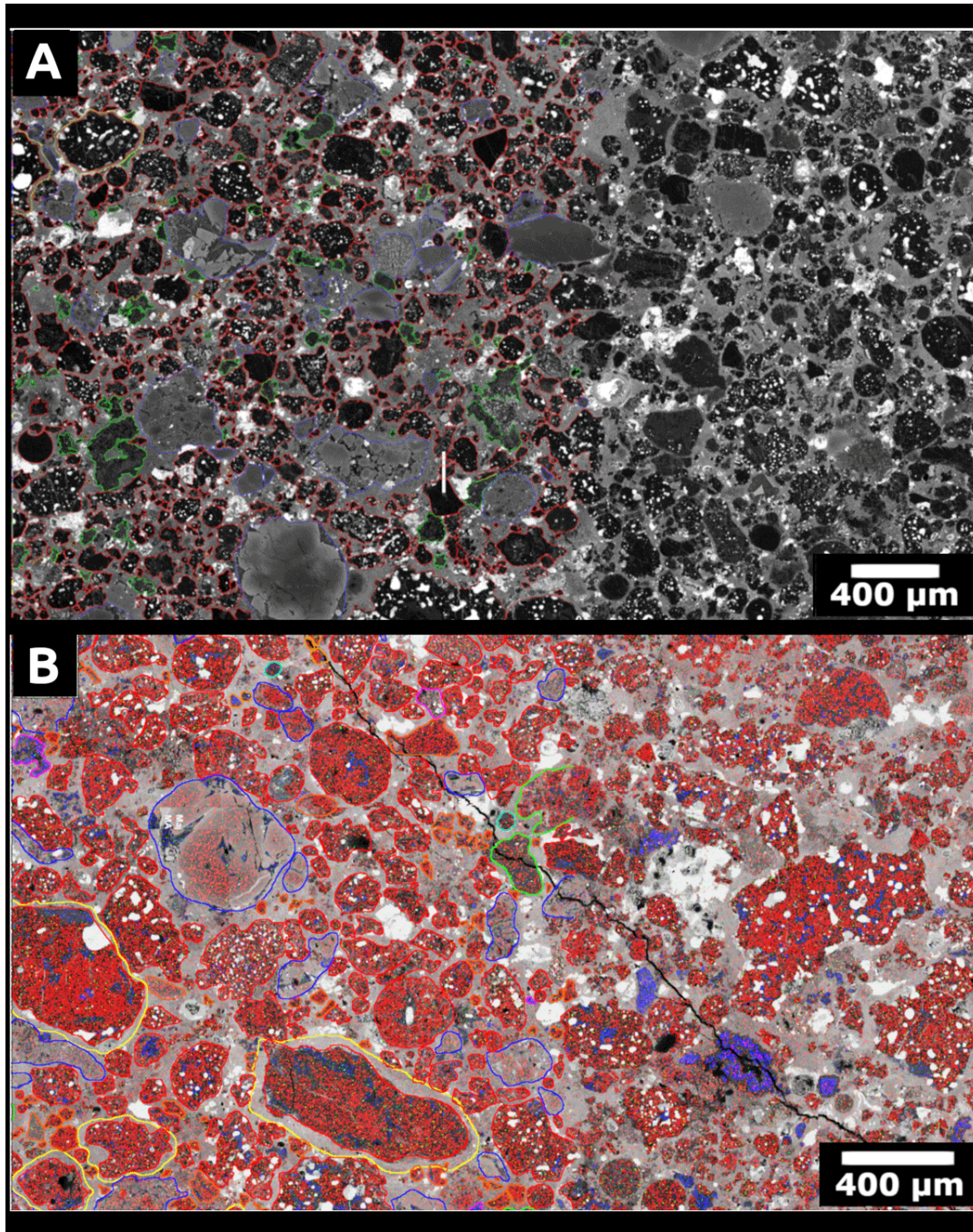
155 Our results show a significant difference between the mean spherical diameters of
156 type-I and type-II chondrules: 92.78 and 162.52 μm, respectively (Table 2). The mean
157 spherical diameters (1σ) of type-I chondrules vary among the different COs: those in Lov
158 123, EM 216, EM 463, and Isna have average sizes of 71.6 (56.51), 90.91 (65.61), 111.37

159 (89.44), and 170.81 μm (54.90), respectively (Fig. 2A, Table 2). Similarly, type-II chondrules
 160 and refractory inclusions (CAIs + AOAs) show variable average sizes among the different
 161 COs (Table 2): in LoV 123, EM 216, EM 463, and Isna, type-II chondrules have mean
 162 diameters of 141.64 (112.92), 103.84 (95.26), 164.10 (100.38), and 184.85 μm (80.14),
 163 respectively, and refractory inclusions have mean diameters of 62.63 (39.06), 75.32 (52.80),
 164 109.76 (71.24), and 67.11 μm (47.81), respectively. The circularity and the mean aspect ratio
 165 of chondrules in our studied CO chondrites is 0.67 ± 0.15 and 1.60 ± 0.45 , respectively.
 166

167 **Table 1.** Modal abundances (the ratio of component pixel area relative to the total pixel area
 168 of the chondrite, in %) of refractory components and chondrules in the analyzed CO3
 169 chondrites.
 170

Component	LoV 123	EM 216	EM 463	Isna
Type I chondrule	46.74	41.59	33.15	1.85
Type II chondrule	8.64	5.22	7.75	33.26
<i>All chondrules</i>	55.37	46.81	40.90	35.11
CAI A	-	-	0.58	0.66
CAI B	-	-	0.55	0.93
AOA	-	-	2.37	-
<i>All refractory inclusions (RI)</i>	8.60	6.82	3.49	1.59
RI/chondrules ratio	0.16	0.15	0.09	0.05

171



172

173 **Figure 1.** Representative examples of particle selection. (A) BSE image of LoV 123. (B) X-
174 ray compositional map of EM 463, with Mg, Al, Ca, and Fe shown in red, blue, green, and
175 white. The colors of particle outlines indicate component type. In (A) type-I chondrules are
176 outlined in red, type-II chondrules in blue, refractory components in green, IOGs in orange,
177 and fine-grained rims in yellow. In (B), outline colors are as in (A), except that refractory
178 components are distinguished between AOAs in green and CAIs in purple.

179

180

181

182

183

184

185 **Table 2.** The number as well as mean and median diameters (μm) of chondrules and
 186 refractory inclusions in each surveyed section.
 187

Component	LoV 123	EM 216	EM 463	Isna	All CO
<i>Type I chondrule</i>					
n	2210	1140	2539	25	5914
Mean diameter	71.60	90.91	111.37	170.81	92.78
1 σ	56.51	65.61	89.44	54.90	74.92
Median diameter	55.68	71.73	88.56	158.10	72.77
<i>Type II chondrule</i>					
n	109	91	253	318	771
Mean diameter	141.64	103.84	164.10	184.85	162.52
1 σ	112.92	95.26	100.38	80.14	97.33
Median diameter	108.01	73.56	138.00	164.99	138.34
<i>All chondrules</i>					
Mean diameter	74.89	91.86	116.15	183.82	100.47
1 σ	62.11	68.28	89.48	71.62	80.27
Median diameter	57.16	71.80	92.60	164.03	79.00
<i>CAIs+AOAs</i>					
n	221	278	252	92	843
Mean diameter	62.63	75.32	109.76	67.11	81.35
1 σ	39.06	52.80	71.24	47.81	43.08
Median diameter	53.11	61.47	88.63	49.03	64.54

188

189 **4. Discussion**

190 **4.1. Correlation between chondrule-size distribution and degree of metamorphism**

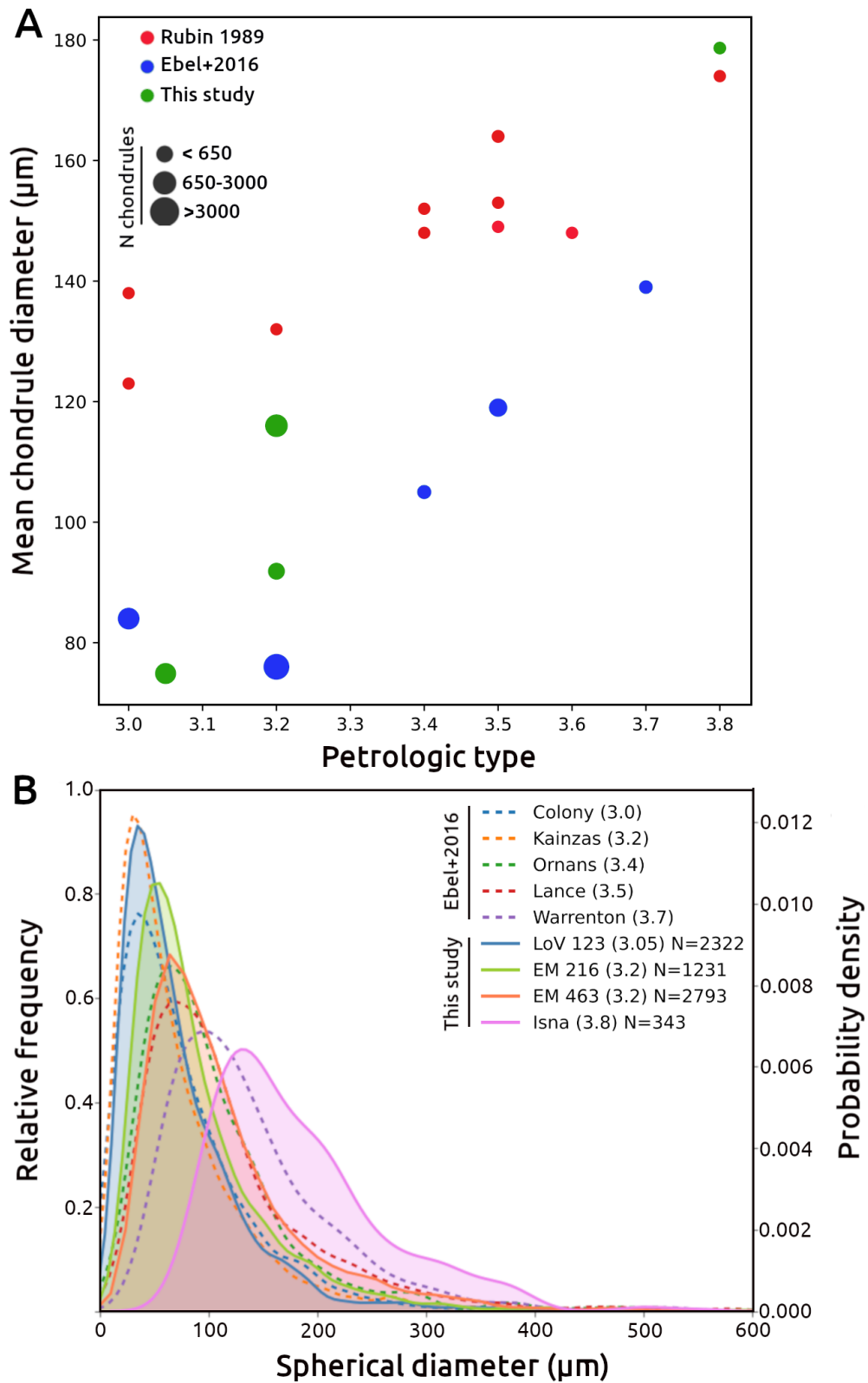
191

192 The degree of thermal alteration (i.e., petrographic grades) experienced by the
 193 carbonaceous chondrites can be estimated based on the mean and standard deviation of Cr_2O_3
 194 content of FeO-rich olivines in type-II chondrules (Grossman and Brearley 2005, Table S1).
 195 We determined a petrographic grade of LoV 123, EM 216 and EM 462 to be 3.05, 3.2 and
 196 3.2, respectively. The petrographic grade of Isna has been determined to be 3.75 ± 0.05 based
 197 on the Cr_2O_3 content of Fe-rich olivines (Rubin & Li 2019) and detailed petrographic and
 198 mineralogical studies of AOAs (Chizmadia et al. 2002). Incorporating recent literature data
 199 for CO chondrites (Ebel et al. 2016), average chondrule diameters define a positive
 200 relationship with the petrographic grade of their parent chondrite (Fig. 2). Such a correlation

201 was first noticed by Rubin (1989), although they reported a dissimilar relationship (Fig. 2A),
202 likely due to their different estimation method and limited number of analyzed particles (<
203 1000). Because we used a similar method as Ebel et al. (2016), we here compare our results
204 to their dataset.

205 The deformation of chondrules (Fig. 1) could have either occurred during the
206 evolution of the protoplanetary disk or within chondritic parent bodies. As lobate chondrules
207 are commonly observed in carbonaceous chondrites that experienced minimal secondary
208 deformation (Jacquet 2021) and CO carbonaceous chondrites show low impact-generated
209 metamorphism transformation (Scott et al., 1992), we thus favor a nebular origin for the non-
210 spherical chondrules.

211



212
 213 **Figure 2.** (A) Mean chondrular diameter vs. petrologic type of CO chondrites (data from
 214 Rubin 1989, Ebel et al. 2016, and this study). (B) Probability density function of chondrular
 215 diameters in CO chondrites. Solid lines, this study (N, number of analyzed chondrules);
 216 dashed lines, Ebel et al. (2016).

217 The observed correlation between chondrule diameter and petrographic grade in CO
218 chondrites could result from (i) the conditions of planetesimal accretion (Scott & Jones 1990)
219 and/or (ii) post-accretion thermal metamorphism processes resulting from impacts and/or ²⁶Al
220 decay (Doyle et al. 2015; Vacher et al. 2018; Amsellem et al. 2020; Turner et al. 2021).
221 Although thermal metamorphism could result in mineral coarsening (Huss et al. 2006), this
222 would mainly affect Fe-Ni metal beads and sulfides and would require temperatures >800 °C,
223 significantly hotter than those estimated for CO chondrites (i.e., 300–600 °C; Jones & Rubie
224 1991; Keil 2000; Bonal et al. 2007). This is consistent with the fact that CV chondrules were
225 only affected by Fe-Mg diffusion without any significant size increase, despite having
226 undergone thermal metamorphism at temperatures higher than in CO chondrites (i.e., ≥600
227 °C; Ganino & Libourel 2017). Furthermore, type-I chondrule boundaries are well defined in
228 CO chondrites, even in the most metamorphosed sample investigated here (i.e., CO3.8 Isna).
229 Taken together, these lines of evidence indicate that (i) the size characteristics of chondrules
230 result from their formation processes during the evolution of the disk and (ii) aerodynamic
231 sorting played a key role during the accretion of the CO parent body(ies).

232 Rubin (1989) suggested that the relationship between chondrule size and the degree of
233 metamorphism is related to monotonic changes in the aggregation of materials in the nebular
234 CO reservoir. In this framework, larger chondrules would have been more centrally
235 concentrated in the CO parent body(ies) than smaller chondrules, which could be explained
236 by either simultaneous or sequential accretion of the two chondrule populations (Scott &
237 Jones 1990). Larger chondrules located closer to the center of the CO parent body(ies) would
238 have experienced more protracted thermal metamorphism than smaller chondrules closer to
239 the surface, where heat generated by ²⁶Al decay was more readily evacuated. Aerodynamic
240 sorting during accretion could thus have produce the co-variation of mean chondrule size
241 with both depth and subsequently with metamorphic grade, as observed for CO chondrites.

242 As CO refractory inclusions are smaller than chondrules (Table 2), this process would also
 243 have generated positive relationships between CO metamorphic grade and their (i) bulk
 244 oxygen isotopic compositions and (ii) refractory inclusion/chondrule (RI/C) ratios.
 245 Interestingly, the former has been reported in previous studies (Clayton & Mayeda 1999;
 246 Greenwood & Franchi 2004), and our data confirm that COs with lower metamorphic grades
 247 show higher RI/C ratios than more metamorphosed ones (Table 2). These results confirm that
 248 aerodynamic sorting during accretion concentrated larger chondrules toward the center of the
 249 CO parent body(ies), but smaller chondrules and CAIs were less concentrated at the core.
 250 Based on this conclusion, in the following section we model and discuss which accretion
 251 process best matches these peculiar features of CO chondrites.

252

253 **4.2. Size-sorting during planetesimal formation**

254

255 In this section we attempt to provide a qualitative explanation of the interpretation
 256 discussed above, in which larger chondrules are more abundant than smaller chondrules at
 257 greater depths within the parent planetesimal, and *vice versa*. We first consider the case of
 258 planetesimal formation due to the self-gravitational contraction of a clump of particles.
 259 Before they collapse into each other, the radial density distribution of particles in the group,
 260 $\rho(r)$, is dictated by the equilibrium between gravity and turbulent diffusion of the gas within
 261 the group, resulting in (Klahr & Schreiber 2020a, 2020b):

262

$$263 \quad \rho(r) = \rho(0) \exp[-r^2/(2l_c^2)], \quad (1)$$

264 where

$$265 \quad l_c = 1/3 (\delta/\text{St})^{1/2} H, \quad (2)$$

266 where St is the particle's Stokes number, r is the distance to the center, H is the pressure-
267 scaled height of the gas in the disk, and δ is the non-dimensional coefficient relating the
268 turbulent diffusion coefficient D to the disk's scale height and orbital frequency Ω :

$$269 \quad D = \delta H^2 \Omega. \quad (3)$$

270 For particles smaller than the mean free path of gas molecules, St is proportional to particle
271 size (i.e., the Epstein regime). In the Stokes regime, St is proportional to the square of particle
272 size, although this case is rarely considered (nor would it change the considerations below). If
273 there are particles of multiple sizes in the clump, even if the gravitational potential is set by
274 one dominant particle size, each will follow a radial distribution like (1), with its own value
275 of l_c . Thus, combining Equations (1) and (2), smaller particles have a more distended radial
276 distribution in the clump, whereas larger particles are more concentrated toward the center.
277 This is because, for larger and smaller particle species 1 and 2, respectively, if $St_1 > St_2$, then
278 $l_{c1} < l_{c2}$.

279 We now consider the settling of particles towards the center of the clump, forming a
280 solid planetesimal. Particles are accelerated towards the center, but undergo more and more
281 friction as their sedimentation rate increases; the two forces cancel when a particle attains its
282 terminal velocity (v_t). Particles accelerated in a gas medium rapidly attain the so-called
283 terminal velocity (v_t). The value of the terminal velocity increases approaching the center of
284 gravitational attraction, but the slowest velocity defines the time that the pebble needs to
285 reach the center, and that velocity is set by initial terminal velocity v_{t_i} . Thus, in the following
286 we assume, without introducing much error and to simplify the final formulae, that v_t is
287 constant (but is particle-size dependent) during the whole contraction of the clump.

288 The planetesimal grows over time as more and more particles reach its surface during
289 the sedimentation process. Thus, we can use the accretion timescale T as a proxy for

290 planetesimal radius (not necessarily a linear relationship). In a time interval dT at time T , the
 291 planetesimal receives the particles that were originally in the clump at a distance between r
 292 and $r + dr$ where $r = v_i T$ and $dr = v_i dT$ (here is where the assumption of constant v_i is
 293 handy). At time T all particles from specie i ($i=1$ or 2) come from a spherical shell with radius
 294 $r_i = V_i T$ and thickness $dr = v_i dT$, so the total mass accumulated in planetesimals between
 295 time T and $T + dT$ is $dM_i(T) = 4\pi r_i^2 \rho_i(r_i) dr_i = 4\pi v_i^3 T^2 \rho_i(r_i) dT$. So, the mass ratio of the
 296 particles with index 1 and 2 accumulated in the time interval T to $T + dT$ is:

$$297 \quad \rho_1/\rho_2(T) = (v_{t1}/v_{t2})^3 \cdot [\rho_1(v_{t1}T)/\rho_2(v_{t2}T)], \quad (4)$$

298 where the first term $(v_{t1}/v_{t2})^3$ comes from the ratio of the volumes occupied at time 0 (i.e., at
 299 the beginning of the contraction of the clump) by the particles that sediment onto the
 300 planetesimal surface between T and $T + dT$. Let's now define $x = v_{t1}T/(2 l_{c1}^2)$. Recall that
 301 $v_{t1}/v_{t2} = St_1/St_2$ and $l_{c1}/l_{c2} = (St_2/St_1)^{1/2}$. Thus, $(v_{t2}T)^2/(2l_{c2}^2) = (St_2/St_1)^3 x^2$. By applying the
 302 definition (1) into (4) and substituting for x , the mass ratio of the two population of particles
 303 landing on the planetesimal at time $T = x(2l_{c1}^2)^{1/2}/v_{t1}$ is:

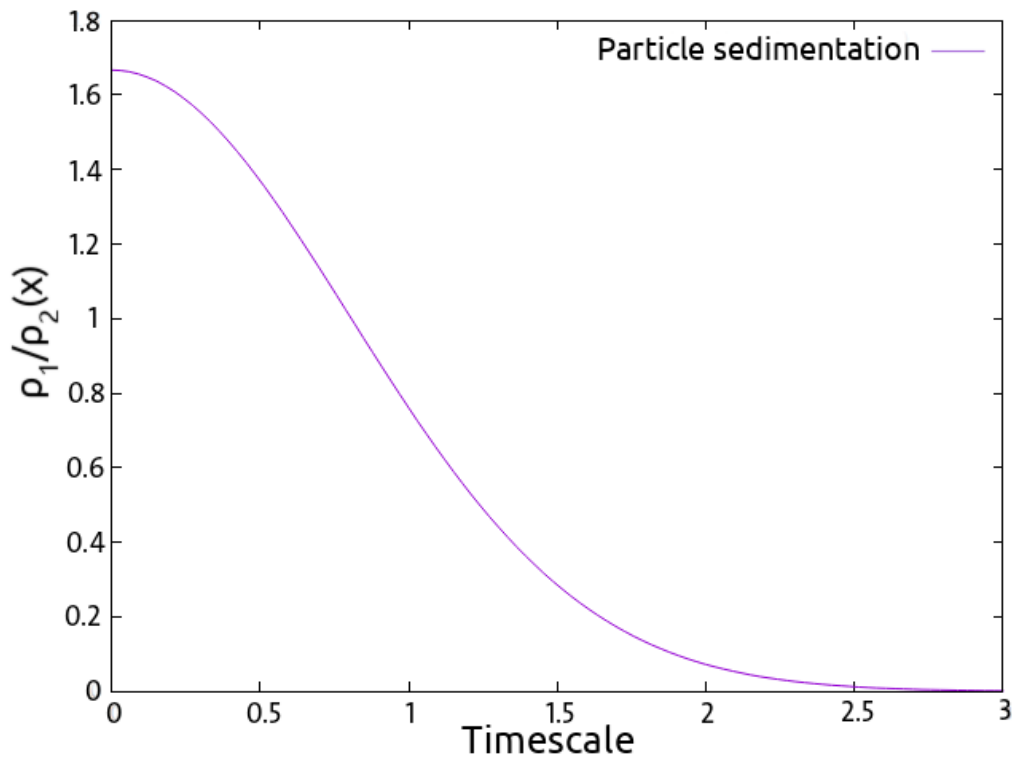
$$304 \quad \rho_1/\rho_2(x) = \rho_1(0)/\rho_2(0) \cdot (St_1/St_2)^3 \cdot \exp[-x^2]/\exp[-(St_2/St_1)^3 x^2]. \quad (5)$$

305 As an example, Figure 3 shows this function for $St_2 = 0.6St_1$, which is appropriate for
 306 comparing chondrules with diameters of ~80–130 μm , i.e., in the Epstein regime.

307

308

309



310

311 **Figure 3.** Equation (5) normalized to the ratio $\rho_1(0)/\rho_2(0)$ at the center of the particle clump
 312 from the beginning of a gravitational contraction leading to the formation of a planetesimal.

313
 314
 315
 316

Our model shows that the ρ_1/ρ_2 decreases monotonically as time progresses (i.e., when
 317 the timescale increases). This is in qualitative agreement with our interpretation that average
 318 chondrule size increases with depth in the parent body. Of note, chondrules are small
 319 compared to pebbles (i.e., 80-130 μm ; Table 2) and would have Stokes number of 1×10^{-4} at
 320 2 AU for 100 μm particle-size (considering a minimum mass solar nebula). This is smaller
 321 than what is typically considered in gravitational collapse models of planetesimal formation
 322 (e.g. Yang et al., 2017). To have a more $\text{St} = 1\text{e-}3$, as more traditionally considered, the gas
 323 should have been depleted by a factor of 10. This may well be possible, because chondrites
 324 formed at a late time (2-3 My) in the disk's chronology, well after the formation of Jupiter
 325 (Kruijer et al., 2017); cavity opening by Jupiter and photo-evaporation may well have
 326 reduced the density of gas by one order of magnitude.

327

328 Above, we considered the case of a gravitationally contracting planetesimal, but it is
329 well accepted that after their contraction, planetesimals may have grown through pebble
330 accretion, as discussed by Johansen et al. (2015). If a planetesimal accreted particles in the
331 Bondi regime, the Stokes number of the preferentially accreted pebbles increases with the
332 planetesimal's Bondi time, which is proportional to the planetesimal's mass (Lambrechts &
333 Johansen 2012). This predicts that larger chondrules should have been predominant at
334 shallower depths in their parent planetesimal, opposite to our observations. In the case that a
335 larger protoplanet scattered a planetesimal into an orbit of greater inclination, the size of
336 particles accreted by the planetesimal would have suddenly decreased because only small
337 particles were available away from the disk's midplane. However, the mass accreted should
338 have also declined, such that small particles would dominate only in a very thin surface layer
339 (Johansen et al. 2015). We do not observe such a drastic change in chondrule size among the
340 studied meteorites of different petrologic types, but rather a gradual trend. Thus, we conclude
341 that our observations are consistent with the formation of the CO parent body(ies) *via* the
342 contraction of a self-gravitating clump of chondrules of various sizes, and that the subsequent
343 growth of the parent body(ies) due to pebble accretion was insignificant.

344

345 **5. Conclusions**

346

347 Our particle-size analysis of CO carbonaceous chondrites revealed that the mean
348 spherical diameters of chondrules increase with increasing metamorphic degree. Combining
349 our results with literature data, we show that this relationship was not established during post-
350 accretion thermal metamorphism, but instead records aerodynamic size-sorting of particles
351 during the accretion of the CO parent body(ies). By modeling the self-gravitating contraction
352 of clumps of chondrules, we show that the accretion processes generated a gradual change in

353 chondrule size, with larger chondrules being more centrally concentrated in the parent
354 body(ies) than smaller ones. Our results also suggest that any subsequent planetesimal growth
355 by pebble accretion should have been insignificant. We thus conclude that our observations
356 are consistent with the formation of the CO parent body(ies) via the contraction of a self-
357 gravitating clump of chondrules, supporting the theory that the formation of planetesimals
358 occurred via gravitational collapse.

359

360 **Research data**

361 Original data from this study are available on the Ordar database;
362 <http://doi.org/10.24396/ORDAR-68>

363

364 **Acknowledgments**

365

366 We thank Johan Villeneuve, Nicolas Schnuriger, and Laurette Piani for helpful
367 discussion. G.A.P and F.O.E. acknowledge support from FONDECYT project 1201223.
368 G.A.P. was supported by an Eiffel excellence scholarship (grant 968045D). We thank the
369 anonymous review for helpful comments and Frederic Rasio for editorial handling. This is
370 CRPG contribution #2777.

371

372

373

374

375

376

377

379 **Table S1.** Chemical compositions of ferroan olivine grains in type-II chondrules of three CO
380 carbonaceous chondrites (EM 463, EM 216, LoV 123).

CO3	#	SiO ₂	FeO	Al ₂ O ₃	CaO	MnO	MgO	Cr ₂ O ₃	TiO ₂	Total
EM 463	49	38.34	27.85	0	0.09	0.31	34.58	0	0	101.2
		36.05	39.18	0.03	0.11	0.28	24.89	0.15	0	100.7
		37.41	30.69	0.05	0.09	0.25	31.50	0.05	0	100.0
		36.48	33.55	0.16	0.08	0.28	30.73	0.09	0	101.4
		38.51	23.92	0.03	0.01	0.31	38.32	0.01	0	101.1
		38.27	26.49	0.10	0.02	0.30	36.47	0.01	0.01	101.6
		37.83	28.32	0.10	0.14	0.34	35.69	0.14	0.01	102.6
		38.53	24.64	0.04	0.11	0.35	37.80	0	0	101.5
		37.00	31.29	0.05	0.14	0.40	31.79	0.06	0.01	100.7
		39.12	23.16	0.04	0.13	0.26	39.32	0.06	0	102.1
		35.92	35.52	0	0.11	0.36	28.72	0.03	0	100.7
		37.92	26.29	0.01	0.15	0.38	36.24	0.08	0	101.1
		37.91	30.51	0.06	0.09	0.17	32.96	0.08	0.01	101.8
		36.94	34.02	0.09	0.02	0.38	29.42	0.18	0	101.0
		39.29	23.36	0	0.18	0.25	38.18	0.19	0.04	101.5
		40.21	17.47	0.10	0.10	0.22	42.78	0.11	0	101.0
		37.97	24.12	0.23	0.30	0.26	36.13	0.57	0.01	99.6
		38.61	26.09	0.02	0.12	0.37	35.62	0.08	0.01	100.9
		38.40	24.24	0.09	0.09	0.16	36.61	0.08	0	99.7
		38.40	26.45	0.03	0	0.22	35.04	0.05	0	100.2
		37.89	30.34	0.04	0.09	0.38	33.23	0.09	0	102.1
		38.34	25.83	0	0.04	0.20	35.77	0	0.02	100.2
		39.23	21.67	0.01	0.03	0.27	39.77	0.12	0	101.1
		38.30	28.82	0.08	0.13	0.43	33.43	0.16	0	101.4
		37.41	31.61	0	0.18	0.31	31.75	0.04	0.03	101.3
		38.65	23.64	0.03	0.02	0.12	38.09	0.12	0	100.6
		38.63	24.94	0.10	0.06	0.16	37.24	0.19	0.01	101.3
		38.24	27.19	0.08	0	0.30	35.15	0.38	0	101.3
		38.28	27.97	0.10	0.01	0.26	33.84	0.05	0	100.5
		40.41	17.10	0.03	0.07	0.22	44.05	0.03	0.03	101.9
		37.81	29.89	0.06	0.17	0.28	32.57	0.10	0	100.9
		36.27	37.11	0.02	0.10	0.48	27.79	0.07	0	101.8
		36.66	33.88	0.07	0.14	0.24	30.13	0.06	0	101.2
		37.74	21.68	0.10	0.06	0.20	40.56	0.10	0	100.4
		37.55	30.09	0.01	0.11	0.22	33.38	0.04	0	101.4
		37.26	32.46	0.08	0.21	0.44	31.28	0	0.05	101.8
		36.82	34.74	0	0.08	0.53	29.35	0.05	0.04	101.6
		35.60	37.13	0.03	0.37	0.19	27.65	0.02	0	100.9
		35.32	40.69	0.02	0.27	0.46	23.44	0.07	0	100.3
		36.00	38.28	0.01	0.18	0.40	26.07	0.07	0	101.0
		37.63	31.64	0.05	0.14	0.43	31.66	0.13	0	101.7

		37.12	34.90	0.04	0.16	0.45	29.55	0.08	0.01	102.3
		38.95	23.89	0.01	0.03	0.16	38.35	0.07	0	101.4
		36.14	37.74	0.04	0.24	0.43	26.92	0.08	0	101.6
		38.19	27.40	0.03	0.14	0.32	35.56	0.15	0	101.8
		36.79	35.39	0.01	0.22	0.39	28.60	0.08	0	101.5
		38.26	28.99	0.01	0.06	0.42	34.50	0.06	0	102.3
		36.28	35.30	0.02	0.24	0.36	28.41	0.06	0.01	100.7
		37.04	29.66	0.03	0.18	0.35	33.41	0.06	0.02	100.7
	Mean	37.71	29.33	0.05	0.12	0.31	33.56	0.09	0.01	
	STD	1.13	5.57	0.05	0.08	0.10	4.57	0.10	0.01	
EM 216	43	37.04	35.98	0.04	0.08	0.41	28.47	0.02	0	102.0
		37.47	33.21	0.03	0.14	0.42	30.91	0.11	0.04	102.3
		36.13	38.93	0.09	0.28	0.39	26.55	0.10	0.01	102.5
		37.49	28.17	0.10	0.22	0.33	35.20	0.08	0	101.6
		38.52	26.03	0.01	0.06	0.30	36.89	0.11	0	101.9
		37.41	31.21	0.03	0.01	0.39	31.99	0.08	0	101.1
		35.96	39.55	0.04	0.25	0.45	24.97	0	0	101.2
		38.79	24.12	0.03	0.02	0.27	37.98	0.41	0	101.6
		37.53	33.13	0	0.15	0.27	32.12	0.09	0	103.3
		37.46	30.82	0.27	0.05	0.24	31.97	0.40	0	101.2
		36.11	39.77	0	0.14	0.22	25.86	0.03	0	102.1
		38.41	28.06	0	0.08	0.29	34.43	0.13	0	101.4
		37.11	34.77	0	0.08	0.47	29.28	0.05	0	101.8
		38.43	25.50	0.03	0.10	0.25	36.57	0	0.02	100.9
		35.91	38.17	0.08	0.19	0.48	25.92	0.19	0	100.9
		37.73	32.52	0.02	0.02	0.22	31.88	0.02	0	102.4
		35.51	41.54	0.06	0.34	0.42	23.33	0.12	0.03	101.3
		36.01	37.16	0.03	0.15	0.46	27.34	0.06	0.02	101.2
		38.80	25.71	0.02	0.11	0.47	37.31	0.04	0	102.4
		36.89	37.57	0.02	0.06	0.37	26.87	0.11	0	101.9
		38.56	26.92	0	0.00	0.13	35.91	0.07	0	101.6
		36.18	38.87	0	0.15	0.35	26.31	0.04	0	101.9
		36.91	31.87	0.08	0.17	0.24	31.28	0.16	0	100.7
		35.93	40.76	0.02	0.22	0.55	24.52	0.05	0.04	102.1
		37.44	32.88	0.06	0.05	0.47	31.49	0.02	0.00	102.4
		35.80	40.93	0.01	0.28	0.38	24.63	0.08	0	102.1
		36.68	37.19	0.02	0.11	0.46	26.80	0.09	0.03	101.3
		37.16	34.65	0.03	0.07	0.32	30.04	0.03	0	102.3
		35.96	39.53	0	0.07	0.19	25.62	0.06	0	101.4
		36.82	36.62	0	0.12	0.32	28.42	0.06	0	102.4
		38.34	28.48	0.04	0.02	0.32	35.09	0.09	0.02	102.4
		36.15	37.60	0.03	0.07	0.32	27.12	0	0.02	101.3
		37.88	30.32	0.01	0.06	0.22	32.70	0.05	0.02	101.2
		38.28	27.78	0	0.05	0.28	35.41	0.17	0	102.0
		34.40	48.35	0.01	0.14	0.45	18.21	0.07	0	101.6
		37.04	34.55	0.04	0.09	0.32	30.23	0.01	0	102.3

		35.51	41.70	0	0.15	0.31	24.15	0.07	0	101.9
		36.93	36.28	0.01	0.13	0.27	28.88	0	0.02	102.5
		36.77	35.47	0.06	0.08	0.29	29.26	0.07	0	102.0
		36.56	35.44	0.06	0.24	0.14	28.97	0.06	0	101.5
		34.61	41.14	0.21	0.25	0.36	23.82	0.40	0	100.8
		37.98	29.72	0	0.10	0.22	33.24	0	0	101.3
		37.46	31.18	0.06	0.10	0.28	33.48	0.18	0.01	102.7
	Mean	36.98	34.42	0.04	0.12	0.33	29.80	0.09	0.01	
	STD	1.09	5.44	0.05	0.08	0.10	4.51	0.10	0.01	
LoV 123	62	35.67	31.03	-	-	0.31	32.75	0.24	0	100.0
		35.54	33.42	-	-	0.31	30.54	0.23	0	100.0
		35.62	32.24	-	-	0.31	32.20	0.27	0.04	100.7
		35.69	33.58	-	-	0.20	31.47	0.27	0	101.2
		33.56	42.69	-	-	0.43	23.09	0.27	0	100.0
		37.40	21.97	-	-	0.25	40.04	0.31	0	100.0
		33.61	41.06	-	-	0.33	25.03	0.32	0.03	100.4
		34.18	36.98	-	-	0.26	28.02	0.40	0	99.8
		36.65	27.88	-	-	0.22	34.58	0.13	0.04	99.5
		35.73	27.90	-	-	0.15	36.32	0.27	0.01	100.4
		35.92	31.78	-	-	0.32	33.20	0.22	0	101.4
		33.28	38.93	-	-	0.59	25.75	0.13	0.01	98.7
		33.17	42.60	-	-	0.34	23.95	0.15	0	100.2
		33.48	42.07	-	-	0.52	24.00	0.13	0.03	100.2
		33.39	41.49	-	-	0.45	24.46	0.36	0.01	100.2
		32.97	42.15	-	-	0.46	24.82	0.25	0	100.6
		37.30	26.38	-	-	0.30	35.92	0.22	0.05	100.2
		40.68	20.79	-	-	0.23	31.63	0.33	0.12	93.8
		34.73	39.52	-	-	0.43	24.90	0.27	0.02	99.8
		34.63	39.66	-	-	0.44	24.74	0.32	0	99.8
		34.68	39.59	-	-	0.43	24.82	0.29	0.01	99.8
		33.82	43.32	-	-	0.49	22.21	0.50	0.02	100.3
		35.19	38.42	-	-	0.46	25.68	0.30	0	100.1
		35.78	29.81	-	-	0.26	33.91	0.32	0.03	100.1
		35.00	34.25	-	-	0.32	29.95	0.21	0.01	99.7
		38.25	18.43	-	-	0.15	42.55	0.75	0	100.1
		34.12	38.47	-	-	0.52	26.47	0.36	0.01	100.0
		34.13	37.41	-	-	0.41	27.88	0.32	0.01	100.1
		34.97	40.21	-	-	0.53	24.48	0.27	0.04	100.5
		34.17	42.01	-	-	0.62	22.93	0.10	0	99.8
		32.64	48.74	-	-	0.53	18.20	0.32	0.02	100.4
		32.33	52.22	-	-	0.61	14.18	0.25	0.03	99.6
		35.88	28.68	-	-	0.25	35.17	0.28	0.03	100.3
		35.78	30.47	-	-	0.39	33.34	0.31	0	100.3
		36.19	30.39	-	-	0.35	32.38	0.59	0	99.9
		36.64	30.31	-	-	0.21	33.17	0.24	0.02	100.6
		37.65	22.20	-	-	0.25	39.53	0.28	0	99.9

37.27	27.96	-	-	0.39	34.91	0.21	0.07	100.8
36.62	28.41	-	-	0.44	34.30	0.22	0	100.0
37.66	23.47	-	-	0.37	38.07	0.38	0.05	100.0
35.49	36.77	-	-	0.32	27.34	0.21	0.04	100.2
35.86	33.14	-	-	0.25	30.56	0.51	0	100.3
36.80	25.71	-	-	0.25	36.44	0.55	0.01	99.7
38.40	17.55	-	-	0.18	43.11	0.23	0.04	99.5
36.00	30.58	-	-	0.36	32.64	0.22	0	99.8
37.61	24.04	-	-	0.22	37.69	0.45	0	100.0
37.93	24.38	-	-	0.30	36.94	0.34	0	99.9
36.08	31.88	-	-	0.34	31.55	0.16	0.03	100.0
33.24	49.31	-	-	0.53	16.72	0.18	0.02	100.0
37.14	24.45	-	-	0.26	37.49	0.23	0.01	99.6
40.74	6.99	-	-	0.11	52.25	0.25	0.02	100.3
36.96	28.77	-	-	0.37	33.99	0.19	0.01	100.3
37.19	25.44	-	-	0.29	37.01	0.29	0	100.2
35.33	38.88	-	-	0.30	25.30	0.26	0.01	100.1
38.64	15.59	-	-	0.35	45.25	0.66	0.03	100.5
38.82	17.52	-	-	0.15	43.18	0.19	0	99.9
39.06	15.93	-	-	0.26	44.54	0.39	0	100.2
38.61	20.66	-	-	0.15	40.72	0.23	0	100.4
35.17	35.55	-	-	0.32	28.56	0.18	0	99.8
34.18	42.09	-	-	0.36	22.67	0.32	0.01	99.6
37.36	21.05	-	-	0.19	40.44	0.49	0.04	99.6
36.10	29.09	-	-	0.23	34.65	0.26	0.05	100.4
Mean	35.88	31.84		0.34	31.62	0.30	0.02	
STD	1.92	9.27		0.12	7.50	0.13	0.02	

381

382

383

384

385

386

387

388

389

390

391 **References**

- 392 Amsellem, E., Moynier, F., Mahan, B., & Beck, P. 2020, *Icarus*, 339
393 Barge, P., & Sommeria, J. 1995, arXiv, <http://arxiv.org/abs/astro-ph/9501050>
394 Bonal, L., Bourot-Denise, M., Quirico, E., Montagnac, G., & Lewin, E. 2007, *GeCoA*, 71,
395 1605
396 Carrera, D., Johansen, A., & Davies, M. B. 2015, *A&A*, 579, 1
397 Clayton, R. N., & Mayeda, T. K. 1999, *GeCoA*, 63, 2089
398 Connolly, H. C., & Jones, R. H. 2016, *JGR*, 121, 1885
399 Chizmadia, L. J., Rubin, A. E., & Wasson, J. T. 2002, *MAPS*, 37(12), 1781-1796.
400 Cuzzi, J. N., Hogan, R. C., Paque, J. M., & Dobrovolskis, A. R. 2001, *ApJ*, 546, 496
401 Cuzzi, J. N., Hogan, R. C., & Shariff, K. 2008, *ApJ*, 687, 1432
402 Doyle, P. M., Jogo, K., Nagashima, K., et al. 2015, *Nat Commun*, 6, 1
403 Drazkowska, J., Alibert, Y., & Moore, B. 2016, *A&A*, 594, 1
404 Ebel, D. S., Brunner, C., Konrad, K., et al. 2016, *GeCoA*, 172, 322
405 Ganino, C., & Libourel, G. 2017, *Nat Commun*, 8, 1
406 Gerbig, K., Murray-Clay, R. A., Klahr, H., & Baehr, H. 2020, *ApJ*, 895(2), 91
407 Greenwood, R. C., & Franchi, I. A. 2004, *M&PS*, 39, 1823
408 Grossman, J. N., & Brearley, A. J. 2005, *M&PS*, 40, 87
409 Huss, G. R., Rubin, A. E., & Grossman, J. N. 2006, *Meteorites early Sol Syst II*, 567
410 Jacquet, E. 2021, *GeCo*, 296, 18-37
411 Johansen, A., Low, M. M. Mac, Lacerda, P., & Bizzarro, M. 2015, *SciAdv*, 1
412 Johansen, A., Oishi, J. S., Low, M. M. Mac, et al. 2007, *Nat*, 448, 1022
413 Johansen, A., Youdin, A. N. D. R. E. W., & MacLow, M. M. 2009, *ArXiv e-prints*.
414 Johnson, B. C., Minton, D. A., Melosh, H. J., & Zuber, M. T. 2015, *Nat*, 517, 339
415 Jones, R. H., & Rubie, D. C. 1991, *EPSL*, 106, 73
416 Keil, K. 2000, *P&SS*, 48, 887
417 Klahr, H., & Schreiber, A. 2020, *ApJ*, 901, 54
418 Klahr, H., & Schreiber, A. 2021, *ApJ*, 911, 9
419 Kruijer, T.S., Burkhardt, C., Budde, G., & Kleine, T. 2017, *PNAS*, 114: 6712-6716.
420 Lambrechts, M., & Johansen, A. 2012, *A&A*, 544, 1
421 Li, R., Youdin, A. N., & Simon, J. B. 2018, *ApJ*, 862, 14
422 Li, R., Youdin, A. N., & Simon, J. B. 2019, *ApJ*, 885, 69
423 Marrocchi, Y., Euverte, R., Villeneuve, J., et al. 2019, *GeCoA*, 247, 121
424 Marrocchi, Y., Villeneuve, J., Batanova, V., Piani, L., & Jacquet, E. 2018, *EPSL*, 496, 132
425 Nesvorný, D., Li, R., Youdin, A. N., Simon, J. B., & Grundy, W. M. 2019, *Nat Astron*, 3,
426 808
427 Ormel, C. W., & Klahr, H. H. 2010, *A&A*, 520, A43.
428 Rubin, A. E. 1989, *Meteoritics*, 24, 179
429 Rubin, A. E., & Li, Y. 2019, *Geochemistry*, 79(4), 125528.
430 Schindelin, J., Arganda-Carreras, I., Frise, E., et al. 2012, *Nat Methods*, 9, 676
431 Scott, E. R. D., & Jones, R. H. 1990, *GeCoA*, 54, 2485
432 Scott, E. R., Keil, K., & Stöffler, D. 1992, *GeCoA*, 56(12), 4281-4293.
433 Simon, J. B., & Armitage, P. J. 2014, *ApJ*, 784, 1
434 Turner, S., McGee, L., Humayun, M., Creech, J., & Zanda, B. 2021, *Sci.*, 371, 164.
435 Vacher, L. G., Marrocchi, Y., Villeneuve, J., Verdier-Paoletti, M. J., & Gounelle, M. 2018,
436 *GeCoA*, 239, 213
437 Wahlberg Jansson, K., & Johansen, A. 2014, *Proceeding Asteroids, Comets, Meteors* 573
438 Wahlberg Jansson, K., & Johansen, A. 2017, *MNRAS*, 469, S149
439 Yang, C. C., Johansen, A., & Carrera, D. 2017, *A&A*, 606

440 Youdin, A. N., & Goodman, J. 2005, ApJ, 620, 459
441